Wiley
Advances in Polymer Technology
Volume 2025, Article ID 4322238, 10 pages
https://doi.org/10.1155/adv/4322238

WILEY

Research Article

Prediction of a Broad Spectra of Membrane Morphologies Through a New NIPS Thermo-Kinetic Model

Marta Romay[1], **Ane Urtiaga**[1], **and Nazely Diban**[1,2]

[1]*Department of Chemical and Biomolecular Engineering, Universidad de Cantabria, Avenue. Los Castros s/n, Santander 39005, Spain*
[2]*Cell Biology of the Nucleus Research Group, Instituto de Investigación Marqués de Valdecilla (IDIVAL), Santander, Spain*

Correspondence should be addressed to Nazely Diban; dibann@unican.es

Received 4 June 2024; Accepted 28 January 2025

Academic Editor: Nasir Ahmad

This work presents a novel semiempirical mathematical approach consisting of a coupled thermo-kinetic model as valuable tool for predicting the polymeric fraction profile of membranes synthesized by nonsolvent induced phase separation (NIPS). Equilibrium binodal curves (BCs) of the system component were incorporated to the Fick's diffusive kinetic model allowing a satisfactory prediction of the tendency to develop symmetric or asymmetric porous membrane morphologies, as well as a fair quantification of average porous fraction profiles. The model was validated using two different ternary systems: (i) polycaprolactone (PCL)/N-methylpyrrolidone (NMP)/water (W) characteristic of instantaneous demixing (asymmetric finger-like porous cross-section morphology); and (ii) PCL/NMP/isopropanol (IPA) characteristic of delayed demixing (symmetric sponge-like cross-section morphology). The loading of graphene oxide (GO) in the quaternary system PCL/GO/NMP/IPA also gave rise to a sponge-like porosity, characteristic of delayed demixing systems, which was reasonably predicted by the coupled thermo-kinetic model developed in this study. In addition, a computational scanning electron microscopy (SEM) image processing methodology was developed to validate the thermo-kinetic model, resulting in an advantageous tool for that purpose. Overall, this work reveals the usefulness of the new thermo-kinetic mathematical approach as a facile computational tool for membrane manufacturers and researchers for a preliminary discrimination of component combinations in quaternary polymer/nanofiller/solvent/nonsolvent NIPS systems.

Keywords: nonsolvent induced phase separation; membrane polymer fraction profile; quaternary systems; SEM image processing; thermo-kinetic modeling

1. Introduction

Polymeric membranes functionalized with nanofillers are employed in multiple fields such as wastewater treatment, tissue engineering (TE), or gas separation among others. The type of application defines the membrane morphology needed. In the field of TE, a branch of bioengineering aiming at the repair, replacement, or regeneration of impaired tissues or organs [1], polymeric membranes have been used as scaffolds for cell proliferation and tissue regeneration [2]. Biocompatible polymer materials are required to contribute positively to cell viability. For instance, polycaprolactone (PCL) has been widely used in the TE field, due to its biocompatibility. In our previous works, homogeneously porous flat PCL membranes undoped and doped with graphene-based nanomaterials (GBNs) were synthesized by non-solvent induced phase separation (NIPS), and it was proved that the presence of graphene oxide (GO) favored the differentiation of neural cells in TE studies [3, 4].

NIPS is a flexible synthesis methodology to produce membranes with a variety of morphological features and porosity, due to its wide diversity of processing variables (i.e. materials, composition, and process temperature). Several works have studied the influence of using different solvents (dimethyl fluoride (DMF), dimethyl sulphoxide (DMSO), N-methyl

pyrrolidone (NMP), dimethylacetamide (DMAc), etc.) [5], as well as various coagulants (water (W), methanol, glycerol…) [6] that induced a variety of membrane morphologies. Furthermore, the loading of a filler induce changes in membranes morphology produced by NIPS, therefore complicating the optimal selection of membrane synthesis variables [5] that is traditionally done based on literature revision, previous experience or ultimately on trial-and-error experiments. This is an unsustainable approach, highly time- and reagent-consuming [7].

Several studies attempted to understand the principles of membrane formation, either by experimental observation or through mathematical models [8], seeking to systematize the selection of the components, so that NIPS-prepared membranes acquire the adequate porous structure and function [9–12]. On this regard, different kinetic models ranging from the macroscopic to the atomistic scales have been developed [8, 13]. Mechanistically rigorous kinetic models, mostly developed for ternary systems, aim mainly to understand the complex phenomena that occur during membrane formation, since this is unfeasible to study experimentally. However, they are of low practicality for fast screening of solvent/nonsolvent pairs. Therefore, an engineering compromise between accurate phenomenological description and fair morphological simulation is advisable [8]. Accurate phenomenological description has a major impact on mesoscopic phase field kinetic models or molecular scale simulations such as dissipative particle dynamics, where grain coarsening and growth kinetics that follow the phase-separation kinetics are modeled for a visual morphological prediction of the membrane structure in a scale of time limited to few seconds, which make it difficult the practical evaluation of the immersion process [14]. Meanwhile, macroscopic finite difference methods usually focus on the phase-separation kinetics to predict porous fraction profiles, as the onset time of demixing has been previously observed to have an important impact on the membrane structure and porous fraction [15]. Therefore, kinetic models based on finite difference methods have been the most popular in the literature as they describe membrane formation in a realistic temporal–spatial scale [8].

Kinetic models typically incorporate fast local equilibrium conditions considering instantaneous demixing and spinodal decomposition. However, the thermodynamics of ternary, and more recently quaternary, systems contain crucial information [5, 16–18] such as the affinities between the components and the composition of the regions that present thermodynamic stability/instability to help discern comparatively the most favorable combination of components for a given NIPS-prepared membrane. This information is omitted in previous kinetic models. Thus, the work of Khansary et al. [14] is particularly interesting, where the information of the thermodynamic phase diagram of a cellulose acetate/acetone/W system was coupled to kinetic mechanisms reporting for the first time a rigorous combined thermo-kinetic model. Authors employed a compressible regular solution (CRS) free energy theory in the phase diagram construction. The main attribute of CRS models is that they only require pure properties of the thermodynamic calculations. As a drawback, although mechanistically insightful, the thermo-kinetic model is too complex and implies high computational cost that is again not advisable for a fast screening of the variables involved in membrane synthesis. Furthermore, although it was proposed to apply it in a cellulose acetate system, this model was not experimentally validated. Conversely, Flory–Huggins (FH) lattice model is more popular in the literature than the CRS, due to its simplicity and ability to incorporate empirical improvements of the binary interaction parameters to fit the experimental results [13]. In example, FH has been extensively used to model the thermodynamics of membrane-forming polymers such as polysulfone, polyethersulfone (PES), polyvinylidene fluoride (PVDF), and so forth in ternary [16, 17, 19] and in quaternary systems such as PVDF/GO and PES/GO [5]. Similarly, kinetic models are usually validated with classical polymer membrane systems (i.e. PES, PVDF, or cellulose acetate), traditional aprotic solvents (NMP, DMAc, and acetone) and typically W as nonsolvent [8, 13–15].

With all the above in mind, this work aims at evaluating the validity of a semiempirical model combining the thermodynamic information and considering a simple diffusive kinetics of the phase separation to preliminary predict the membrane porous profile under a broad variety of morphological casuistic of phase-separated membranes including ternary and quaternary systems. To validate the model, the predicted morphology was compared to that obtained experimentally in ternary and quaternary systems of PCL/GO/NMP/coagulant with interest in TE [4, 20]. Ternary phase-separation systems of PCL/NMP/coagulant, focused on the comparison of the use of W as coagulant, which presents instantaneous demixing, and isopropanol (IPA) with a delayed demixing. For the numerical comparison of simulated and experimental membrane polymer fraction profiles a computational scanning electron microscopy (SEM) image processing methodology was implemented.

2. Mathematical Model

Motivated by the search of mathematical simplicity, in the present study a modification of the model by Fernandes et al. [12] based on Fick's law, later adopted by Wang et al. [21], has been used.

Figure 1 depicts the schematics of the mass transfer during NIPS. Two regions can be found: region A or polymer solution, ($j = A$) and region B or coagulation bath, ($j = B$); and three compounds: nonsolvent ($i = 1$), solvent ($i = 2$), and polymer ($i = 3$). At time $t = 0$, (Figure 1a) region A is composed of solvent and polymer, and region B is made of nonsolvent. Immediately after membrane immersion in the coagulation bath, the exchange between the solvent and the nonsolvent begins: the nonsolvent diffuses inside the polymeric solution ($J_{1,A}$), while the solvent diffuses across the membrane ($J_{2,A}$) and then, after crossing the polymer solution boundary, through the coagulation bath ($J_{2,B}$). The increase of nonsolvent content and the reduction of the solvent concentration increases the polymer viscosity in the polymer solution. Later, when the composition of the system reaches thermodynamic equilibrium, the system separates into two phases, thus

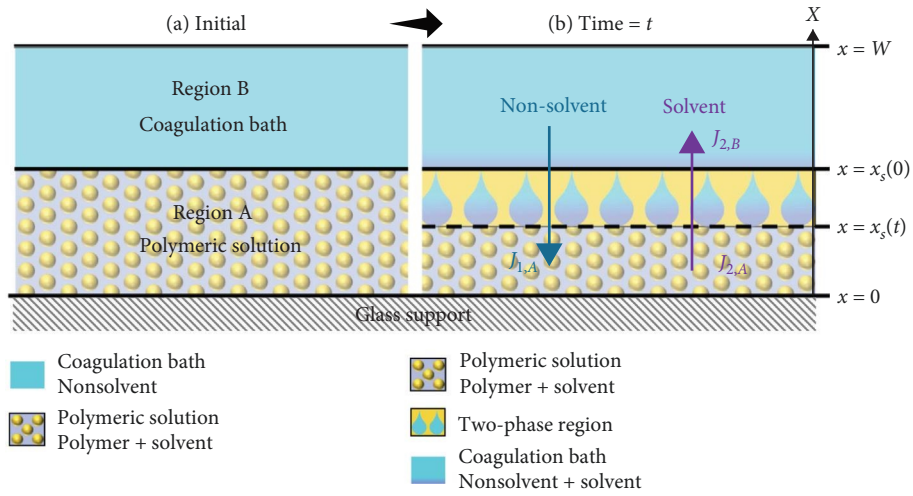

FIGURE 1: Mass transfer exchange of NIPS process across the membrane thickness position x. (a) At the beginning of the contact between polymer and coagulation solutions. (b) After certain time t of contact.

defining the pore structure (Figure 1b). To include thermodynamics, a mobile equilibrium diffusion boundary is proposed (x_s).

For the mathematical description of the coupled thermokinetic model, the following assumptions and simplifications were done:

a. Mass transfer is considered only in x-axis dimension (Figure 1).
b. There is no polymer diffusion in the coagulation bath, $J_{3,A} = 0$, albeit there is a change in its volume fraction in region A.
c. Convective movement of the polymer and the GO components is neglected.
d. Due to the rapid immersion in the coagulation bath after casting, solvent evaporation can be neglected.
e. Exchange kinetics is sufficiently slow to reach immediate phase equilibrium separation once the compositions touch the binodal curve (BC)-forming polymer nucleus [22]. Once the components composition at the interfacial diffusion boundary node or phase-separation front (x_s) reaches the BC (onset time of demixing), the x_s-boundary node is moved to the next x-node ($x_s - 1$) and the process is repeated up to the final node $x_s = 0$ denoting the whole membrane thickness.
f. Kinetics of the growth and coarsening of the polymer nucleus has negligible qualitatively influence on the local polymer fraction.

Ficks's second law is used to describe the molecular diffusion of the compound i through the phase j:

$$J_{(i,j)} = \frac{\partial \phi_{(i,j)}}{\partial t} = D_{i,j} \cdot \frac{\partial^2 \phi_{(i,j)}}{\partial x^2} \quad \begin{cases} i = 1, 2, \text{for } j = A \\ i = 2, \text{for } j = B \end{cases} \tag{1}$$

$J_{(i,j)}$ in (s^{-1}) being the flux, $\phi_{i,j}$ the molar volume fraction composition (nondimensional) and, $D_{i,j}(m^2/s)$ the diffusion coefficient, in all cases of component i in region j, and x the direction of mass transfer.

Equations (2) and (3) are Neumann boundary conditions to describe the absence of flux in the glass casting support ($x = 0$) neither beyond the external surface of the coagulation bath ($x = W$), corresponding to the boundaries of the system.

$$\left.\frac{\partial \phi_{(i,j)}}{\partial x}\right|_{x=0} = 0 \quad i = 1, 2 \quad \text{for } j = A \tag{2}$$

$$\left.\frac{\partial \phi_{(i,j)}}{\partial x}\right|_{x=W} = 0 \quad i = 2 \quad \text{for } j = B. \tag{3}$$

The following continuity condition is fulfilled at both sides of the membrane interface:

$$D_{i,A} \cdot \left.\frac{\partial \phi_{(i,A)}}{\partial x}\right|_{x=x_s} = D_{i,B} \cdot \left.\frac{\partial \phi_{(i,B)}}{\partial x}\right|_{x=x_s} \quad i = 1, 2. \tag{4}$$

At the polymer solution–coagulation bath interphase there is a rapid thermodynamic equilibrium of mixing between the solvent and coagulant, represented in the present work through the simplified expression set out in Equation (5), where k_i represents a partition coefficient if the component i either the nonsolvent ($i = 1$) or the solvent ($i = 2$). The literature proposes a value of 0.4 for W (also valid for low molecular weight alcohols), indicating a restriction for the coagulant molecules to enter to the highly viscous polymer solution, and 1 for NMP (or other organic solvents), rapidly mixed with the aqueous solution or coagulation bath [12, 21].

$$\left.\phi_{(i,A)}\right|_{x=x_s} = k_i \cdot \left.\phi_{(i,B)}\right|_{x=x_s} \quad i = 1, 2. \tag{5}$$

From the mass balance, Equation (6), the volume fraction of polymer in the polymer region ($\phi_{3,A}$), Equation (7), and the volume fraction of nonsolvent in the coagulation bath ($\phi_{1,B}$), Equation (8), can be obtained:

$$\sum_{i=1}^{NC} \phi_{i,j} = 1 \tag{6}$$

$$\phi_{3,A} = 1 - \phi_{1,A} - \phi_{2,A} \tag{7}$$

$$\phi_{1,B} = 1 - \phi_{2,B}. \tag{8}$$

For the kinetic calculation of the quaternary system, it is considered that during demixing the additive (GO) remains with the polymer fraction, so the mass of both components is added to calculate $\phi_{3,A}$.

It has been previously experienced that the membrane morphology is ultimately decided by the point of entry into the miscibility gap, that is the onset of phase separation where polymer-rich and polymer-lean compositions are first stablished in the moment the components composition crosses the BC [14, 15]. Phase separation is generally considered to be immediate, as the delay in reaching this equilibrium cannot be determined experimentally and the choice of an equilibrium delay time would be arbitrary. From this observation arises the main simplification of the present model, that is assumption (f).

The location of the BCs on the ternary plot is characteristic of each component system, impacting the displacement of the miscibility gap and therefore affecting the rate in which the thermodynamic instability of the solution is reached [5]. The present model incorporates the mathematical description of the BC that establishes the boundaries between the compositions of the homogeneous and heterogenous phases. The phase-separation BCs were modeled using a semiempirical FH thermodynamic model for ternary systems reported in our previous work [19] and expanded for quaternary systems in Appendix A of the Supporting Information. As reported, this FH model incorporates a ternary interaction parameter that is estimated by experimental fitting of cloud points (CPs). This approach avoids the need of correction factors for binary interaction parameters reducing therefore the number of fitting parameters.

As a simple procedure to account for the thermodynamic phase equilibrium in the kinetic model, the modeled BC in ternary systems or the spinodal curve (SC) in quaternary systems, attained with the optimization procedure described in Appendix A (Supporting Information), was linearized using Equation (9) as proposed by Boom et al. [23]. Details about the linearization procedure and the values of the linear fitting parameters are reported in Appendix D of the Supporting Information.

$$\ln\frac{\phi_1}{\phi_3} = b \cdot \ln\frac{\phi_2}{\phi_3} + a. \tag{9}$$

Equation (9) was incorporated to the kinetic model in a cyclic comparative loop where the dynamic change by diffusion of the polymer-rich phase composition at the separation front $\phi_{(i,A)}|_{x=x_s}$ is iteratively compared to all components compositions (polymer, solvent, and nonsolvent) calculated with Equation (9). When the composition lies over or crosses from the homogeneous to the heterogeneous region established by the linearized BC (Figure D1 in Appendix D in the Supporting Information), the phase-separation equilibrium is set, and the nuclei formation starts from the polymer-rich composition. At this moment, the phase-separation front (x_s) moves to the next x node in the polymer solution region and the iterative comparison between the diffusional change of compositions and the equilibrium separation compositions is repeated. This procedure continues until the phase-separation front (x_s) reaches the glass support ($x = 0$).

According to references [12, 21], the diffusivities of the solvent and the coagulant in region A is considered in the order of 10^{-12} m^2/s due to the high viscosity of this solution. Meanwhile, in region B the values of diffusion coefficients are 2 orders of magnitude higher (10^{-10} m^2/s). Certain models account for the variation with time of diffusion rates in the polymeric region [24, 25]. Although during the phase inversion there is a progressive increase in the viscosity of the polymeric solution, the diffusion coefficients considered here are in the solid diffusion range and therefore the influence of its variation has been considered negligible.

The code for the simulations was written in MATLAB language and run on a workstation with two Intel Xeon Gold 6148 processors and 256 GB of RAM. Details on the numerical discretization of the coupled thermo-kinetic model are collected in the Supporting Information, Appendix E.

2.1. Computational Methodology for SEM Image Processing. The experimental validation of the mathematical model was done using a computational methodology for SEM image processing [26]. Figure 2 depicts the flowchart of the steps taken to calculate the polymer fraction profile using the SEM images of the cross section of membranes synthesized in the present work.

The program was developed in MATLAB R2021a and it was used for image processing, curve fitting, and statistics and machine learning toolboxes. Detailed description on the commands and procedure for image processing can be found in the Supporting Information, Appendix F.

3. Experimental

3.1. Materials. As a polymer, poly ϵ-caprolactone (PCL, MW 80 kDa, Sigma Aldrich) was used. For all the preparations, PCL was dried overnight to remove possible moisture. NMP (99% extrapure, Acros Organics) was used as solvent; either ultrapure W or 2-propanol (IPA, 99%, Oppac) were used as nonsolvent or coagulant; GO (Graphenea, S.A.) was used as the filler.

3.2. CP and Precipitation Point Titration. Experimental BCs were obtained at 293 K using CP titration consisting on the addition of drops of nonsolvent (W or IPA) to polymer solutions (PCL/NMP or PCL/NMP/GO) with varying polymer content (3–7 wt.%) continuously stirred until permanent

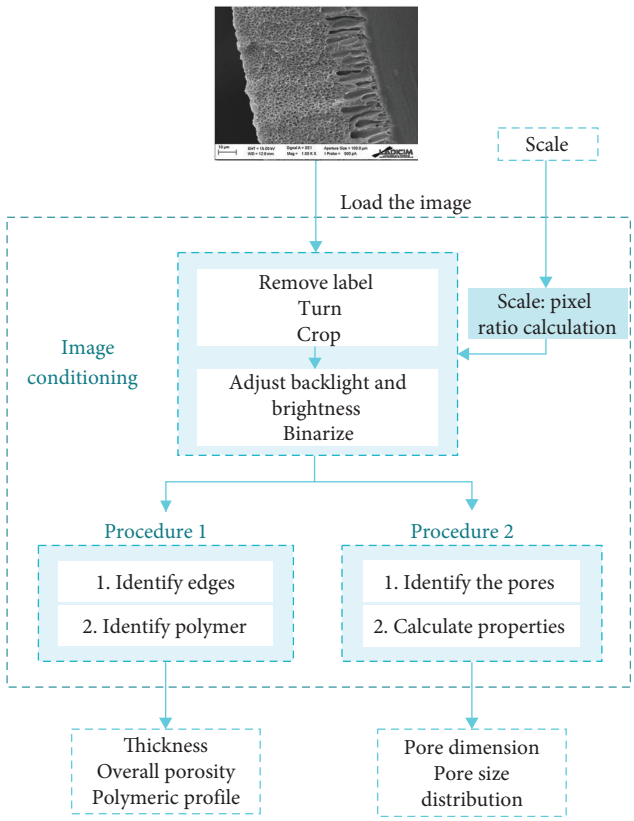

FIGURE 2: Flowchart of SEM Image processing methodology (MATLAB R2021a software).

turbidity was observed. When GO was used, the initial polymer solution was not transparent which difficulted the visualization of CPs formation (BC points). In this case, the precipitation points (PPs) (SC points) were monitored.

3.3. Membrane Synthesis. The synthesis of PCL and PCL/GO membranes by NIPS was done using NMP as solvent, either W or IPA as the nonsolvent, and eventually GO as filler, which procured interesting cues for neural cell differentiation in TE applications, as previously reported [3]. In ternary systems, a polymer solution of 15%wt/wt PCL in NMP was used. For PCL/GO membranes a 0.1%wt/wt of GO was sonicated for 40 min in NMP and then 15%wt/wt PCL was solved in a roller. Proper homogeneous dispersion of GO and stability of PCL/GO solutions were previously tested by observing the absence of GO deposits after 48 or 24 h, respectively, at rest [4, 20]. The use of GO or rGO concentrations higher than 0.1 wt.% produces mechanically fragile membranes not suitable for TE [20]. Furthermore, it was observed experimentally that at 0.5 and 0.8 wt.% GO, the PCL/GO/NMP/IPA solution jellified before the phase separation could be observed, and the CPs of those systems could not be determined experimentally.

The polymer solution at 293 K was cast on a glass support using a doctor blade casting knife (Elcometer) adjusted to a 100 μm thickness and then immediately submerged in the coagulation bath (at 293 K) until complete membrane precipitation. Table 1 collects the codification of the synthesized membranes and the composition of the polymer solutions and coagulation baths.

3.4. Membrane Characterization. Membranes cross sections were characterized by SEM (Carl Zeiss EVO MA 15) at 20 kV. Membranes were fractured after immersion in liquid nitrogen and kept overnight at 30°C under vacuum. Then, the samples were gold sputtered. SEM images were processed using the procedure explained in Section 2.3. These data were used to validate the porous profile predicted by the thermo-kinetic model.

Membrane thickness (δ) was quantified with an electronic micrometer (Standard, Series 293, Mitutoyo). Membrane bulk porosity (ε) was calculated by densimetry using a hydrostatic weighing method consisting on a balance (model MS304TS/00) coupled to a density kit (Standard and advanced, Mettler-Toledo, Spain) and using W as auxiliary liquid. The density of the membrane (ρ_m) was calculated as:

$$\rho_m = \frac{A}{A-B}(\rho_o - \rho_L) + \rho_L, \tag{10}$$

being A the weight of membrane in air, B the weight of membrane in W, ρ_o the W density (0.9982 g/cm^3), and ρ_L the air density (0.0012 g/cm^3). Finally, ε was calculated with Equation (11), being $\rho_P = 1.145 g/cm^3$, the density of the polymer PCL.

$$\varepsilon(\%) = \left(1 - \frac{\rho_m}{\rho_p}\right) \cdot 100 \tag{11}$$

4. Results and Discussion

4.1. Thermodynamic Model and Ternary Interaction Parameter Estimation. The FH thermodynamic model (Appendix A–C) was applied to calculate the BC and SC for the ternary systems PCL/NMP/W and PCL/NMP/IPA and the quaternary system PCL/GO/NMP/IPA. For comparison, Figure 3 presents the simulated BC and SP curves in the pseudoternary phase diagram, as well as the experimental CPs of ternary systems and PPs of the quaternary system corresponding respectively to the BC and SC. Regarding ternary systems, the experimental CPs of PCL/NMP/W are very proximate to the solvent axis, meanwhile the PCL/NMP/IPA CPs are displaced to the right. This displacement indicates that a higher amount of IPA is required to induce the beginning of the polymer nucleation, that is the onset of phase separation, compared to W. This is congruent with the similar radius of interaction (Figure G1 in the Supporting Information, Appendix G) between IPA and PCL ($Ra = 16.6$) versus NMP and PCL ($Ra = 14.8$), pointing out that IPA behaves almost like a solvent for PCL, rather than a coagulant.

The ternary interaction parameters estimated by fitting the experimental CPs to the simulated BCs were $\chi_{123} = -0.89$ for PCL/NMP/W, and $\chi_{123} = 1$ for PCL/NMP/IPA. The negative sign of χ_{123} is associated to an effect of cosolvency between the solvent and the nonsolvent, while positive values indicate

Table 1: Membranes codification and composition of polymer and nonsolvent solutions.

Membrane code	Polymer solution (Polymer (/filler)/solvent)	Coagulation bath
M-W	PCL (15%wt/wt)/NMP	Water (100%wt/wt)
M-IPA	PCL (15%wt/wt)/NMP	IPA (100%wt/wt)
M-GO	PCL (15%wt/wt)/GO (0.1%wt/wt)/NMP	IPA (100%wt/wt)

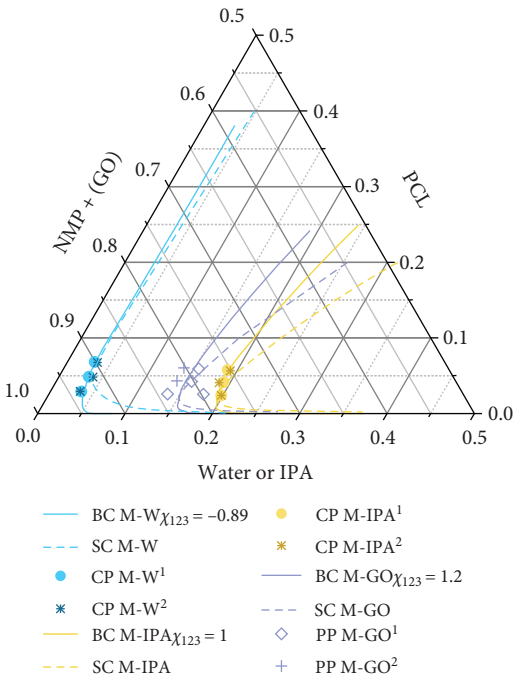

Figure 3: Ternary phase diagram of (1) M-W, (2) M-IPA, and (3) M-GO membrane systems. BC, Binodal curve (continuous line); SC, spinodal curve (dashed line); CP, cloud point; PP, precipitation point. See membranes code in Table 1.

noncosolvency. Cosolvency has been widely described, and occurs when polymers are soluble in mixtures of two nonsolvents, for example: poly (ethylene-co-vinyl alcohol)/2-propanol/W or polystyrene/acetone/diethyl ether [27, 28]. Therefore, ternary interaction parameter values estimated in this study, can be explained by a higher solubility of PCL in NMP/W mixtures at certain compositions than expected in single polymer/solvent systems. Meanwhile, the positive value of the ternary interaction parameter of PCL/NMP/IPA mixtures indicates that the solubility of PCL in the NMP/IPA mixtures is lower than expected in single NMP or IPA solutions. The low solubility of PCL in NMP observed in the Hansen solubility space (Figure G1 in Appendix G of Supporting Information) might be causing the important effect of the ternary interaction parameter in the systems under study [22].

As Figure 3 depicts, the presence of 0.1 wt.% of GO in PCL/NMP/IPA system shifted to the left the BC in the ternary components diagram. Similarly, in PVDF/DMF/W and PES/DMSO/W systems, the addition of 0.1 and 0.5 wt.% of GO led to a subtle displacement to the left of the thermodynamic equilibrium [5]. The hygroscopic character of GO [29] might increase the affinity of the PCL/GO mixture toward the polar–OH group in IPA, which would explain the displacement of the thermodynamic phase equilibria of the quaternary system to the left-hand side of the diagram, compared to the ternary system. The ternary interaction parameter of the quaternary system was estimated by fitting the experimental PPs to the modeled SC, obtaining a value of $\chi_{123} = 1.2$, which confirms the noncosolvency between NMP and IPA previously observed for PCL/NMP/IPA. The deviation from the estimated ternary interaction parameter in the PCL/NMP/IPA system could be attributed to the greater experimental dispersion of the PP for PCL/GO/NMP/IPA systems observed in Figure 3.

In order to demonstrate the validity of the estimated ternary interaction parameters, the experimental and modeled BCs for PCL/NMP/W system at three temperatures (293, 308, and 323 K) are presented in Figure G2 of Appendix G of the Supporting Information. In example, the value of the ternary interaction parameter changes from −0.52 (at 323 K) to −0.68 (at 303 K). A 23% change in the value of the ternary interaction parameter would result in the modeling of a BC that corresponds to a temperature change of 20 K. Therefore, we consider the model has fair sensibility for the estimation of the ternary interaction parameter.

4.2. Simulation and Experimental Validation of the Membrane Porous Profile. Figure 4 a–c shows the membranes cross sections synthesized by NIPS in this work. These images depict the large effect of the nonsolvent (W vs. IPA) on the membrane pore morphology and symmetry that contrasts with the mild effect that the change in the solvents can produce [5]. M-W membranes, which correspond to the ternary system PCL/NMP/W, present the typical finger-like pore structure characteristic of instantaneous (fast) demixing in NIPS. On the other hand, M-IPA and M-GO membranes, both employing IPA as nonsolvent, present a sponge-like porosity characteristic of delayed NIPS demixing. This structure agrees with the location of the BCs in the phase diagram of the ternary and quaternary systems that were obtained in the thermodynamic analysis.

In Figure 4d–f, the distance between the green and blue lines establishes the thickness of the membrane in the SEM images. Table 2 shows the comparison between the membrane thickness measured with a micrometer and the thickness estimated with the SEM image processing. The latter presents higher values for each membrane analyzed, as the thickness estimation depends importantly on the angle adopted by the membrane cross section during the image capture, but in general the SEM values of membrane thickness fairly fall within the variability of measured values. The reduction in membrane thickness during casting and NIPS process observed in our

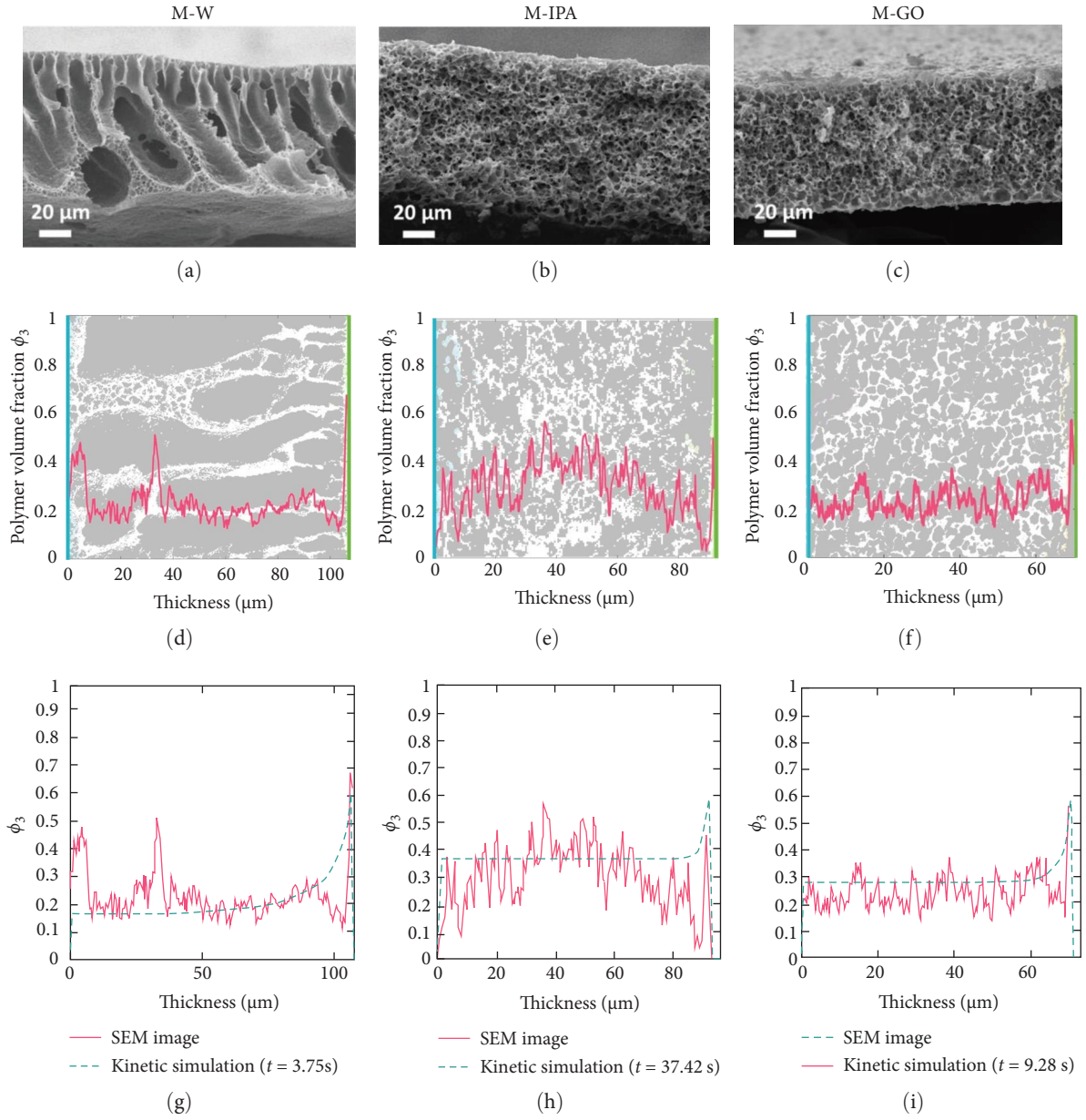

FIGURE 4: (a–c) SEM cross-sectional images of plain PCL ((a) M-W and (b) M-IPA) and composite PCL/GO ((c) M-GO) membranes presenting instantaneous demixing ((a) M-W) and delayed demixing ((b) M-IPA and (c) M-GO). (e,f) Porous profile analysis (red line) of a binarized cross-section image of the membranes (background image) performed with the SEM image processing computational methodology. In images (d–f) green line represents the top layer and blue line the bottom layer of the membranes cross section. (g–i) Comparison of the simulated polymeric profile and the experimental profile analyzed by SEM image processing computational methodology for ternary (g,h) and quaternary (i) systems.

TABLE 2: Comparison of membrane thickness measured with the micrometer and calculated by the SEM image processing methodology.

Membrane	Membrane thickness by micrometer (μm)	Membrane thickness by SEM image processing (μm)
M-W	97 ± 5	107
M-IPA	85 ± 6	92
M-GO	69 ± 2	71

Table 3: Comparison between porosity values simulated with the thermo-kinetic model and experimental values achieved by SEM image processing and densimetry.

Membrane code	M-W	M-IPA	M-GO
Bulk porosity by densimetry (%)	78 ± 1.2	71 ± 0.8	76 ± 1.0
Bulk porosity by SEM image processing (%)	79	71	76
Bulk porosity by thermo-kinetic simulation (%)	79	63	74
Polymer fraction at the top cross-sectional surface by SEM image processing (%)	67	50	56
Polymer fraction at the top cross-sectional surface by thermo-kinetic simulation (%)	60	59	59
Average polymer fraction of internal cross-section by SEM image processing (%)	20	31	25
Average (steady-state) internal polymer fraction by thermo-kinetic simulation (%)	16	36	28

membranes agrees with the theoretical concept proposed by Khansary et al. [30]

The polymer fraction profile attained with the SEM image processing tool shows an irregular profile in all the membranes. This variability is expected, due to the natural stochastic organization of the porosity in real membranes. However, the experimental polymer fraction variability is particularly high in M-IPA, where the polymer volume fraction varied between 0.6 and 0.05, leading to deviation errors as high as 87% between the specific positions of experimental polymer profiles and the simulated curve with the thermo-kinetic model. However, overall it can be observed qualitatively that the M-IPA membrane presents a homogeneous membrane morphology in the SEM image. Due to the fracture of the membrane, the cross-section SEM image presents different planes. The SEM image processing tool is biased by the different contrast of the image and considers the deeper planes as a big pore causing artifacts in the quantitative values estimated. Therefore, the quantitative data of the experimental profile of polymer volume fraction estimated by the SEM image processing tool must be carefully considered and the point-by-point results cannot be considered as the sole basis for determining the validity of the mathematical model predictions. Nevertheless, the average values attained with the SEM image processing tool are of utility for the semi-quantitative analysis of the polymer fraction profile and its comparison with the simulated values. The porous fraction profiles analyzed from SEM images reported by Wang et al. [21] in poly (latide-co-glycolide) membranes synthesized by NIPS using W as coagulant are fairly similar to our M-W membranes, presenting a finger-like morphology and porous fraction profiles decreasing from ~0.45 in the membrane surface down to 0.15 in-depth of the membrane cross section.

Average quantitative results of the polymer fraction profiles achieved with the SEM image processing tool (Figure 4d–f) are collected in Table 3. The bulk porosity determined by densimetry and SEM image processing showed similar results, ranging between 71% for M-IPA and 79% for M-W. The experimental values fall within the range of values of membrane porosities synthesized by NIPS typically reported for different polymers (PES, PVDF, PCL, etc.), that could be between 30% up to 85% depending on the polymer concentrations and systems employed [3, 5, 31]. The presence of finger-like macropores in M-W membranes is aligned with a higher membrane bulk porosity.

As it can be observed (Figure 4g–i and Table 3), the semi-empirical thermo-kinetic model developed in the present study predicts acceptably well the average polymer fraction profile attained through SEM image processing for ternary and quaternary systems. The polymer fractions at the membranes top surface correspond to maximum values of the polymer profiles as expected. As shown in Table 3, top layer polymer fractions were ranging between 59% and 60% in the simulations of the thermo-kinetic model, and between 50% and 67% with the SEM image computational analysis. The polymer fraction in the top surface is strongly affected by the kinetic contribution of the solvent/nonsolvent exchange at the initial moment of contact, that depends on the diffusivities, whose values are very similar in the present work. Therefore, similar polymer fractions in the top layer were simulated for the three membranes (59% and 60%). Improvements on the predictions of the model could be made by incorporating an equation describing the polymer convective displacement inward the membrane domain. Conversely, the internal polymer fractions of the three membranes increase progressively as the BC of the systems shifts to the right of the diagram as follows: 20% by SEM image processing versus 16% attained by simulation with the thermo-kinetic model for the M-W membranes; for the M-GO system the values were 25% versus 28%, and for the M-IPA 31% versus 36%.

As has been observed, all membranes present a decay in polymer fraction between the values at the top layer to those in the internal cross section. The most abrupt polymer fraction decay (44% decay from the simulated data and 47% by SEM analysis) corresponds to the M-W membrane with a clear asymmetric finger-like pore morphology (classical instantaneous demixing) that also presents the shortest elapsing simulation time (3.75 s). M-IPA presents the most homogeneous polymer profile between the top and internal cross section (23% decay simulated vs. 19% by SEM analysis) and the largest elapsing simulation time (37.42 s). Finally, M-GO presented an intermediate drop in polymer fraction and elapsing simulation time (31% decay both by simulation and SEM image processing and 9.28 s of elapsing time). It is worth noting the fair agreement between simulated and experimental elapsed times for membrane precipitation. These comparisons demonstrate the validity of the model predictions in terms of polymer fraction and porous profile for ternary and quaternary PCL-based NIPS systems despite the important mechanistic simplifications

assumed and the inability of mathematical models applying finite difference methods to describe realistic irregular membrane morphologies.

The fair predictive results could be attributed to the positive impact that the kinetic model receives when coupled to the experimentally adjusted thermodynamic phase-separation curves. This might be caused as the different locations of the BC in the pseudoternary system will directly impact the onset time of phase separation in the internal polymer structure and the consequent instantaneous or delayed demixing character of the phase inversion. Therefore, the nonrigorous model presented in this work was able to fairly determine semiquantitatively the porosity profiles of the membranes and instantaneous-delayed demixing character (linked to the asymmetric or symmetric porous structure of the membranes), which was valid not only to ternary systems, but also to quaternary systems containing GBNs to produce polymer-graphene composite membranes.

5. Conclusions

A new thermo-kinetic mathematical model to describe the membrane porous morphology attained by NIPS has been developed. The model has been validated using a PCL/GO/NMP/IPA quaternary system with important application for cell culture scaffolds in TE. The BC (ternary systems) and SC (quaternary systems) were modeled with the FH theory. The incorporation of a linearized expression of the phase equilibrium curves (binodal or spinodal for ternary or quaternary systems respectively) in a kinetic diffusive model allowed a reasonable description of the cross-sectional polymeric fraction profiles of membranes produced by NIPS with instantaneous demixing represented in the PCL/NMP/W system, delayed demixing represented in the PCL/NMP/IPA and intermediate demixing observed in the quaternary PCL/GO/NMP/IPA system, as a consequence of the impact of the location of the BC on the phase-separation onset time.

Importantly, the contribution of the present model is the ability to fairly predict, with a computationally facile and rapid method, a broad range of porous membrane morphologies applicable not only to ternary systems, but also to quaternary systems. Significantly, the major benefit of the present thermo-kinetic model would be the simplification on the number of NIPS component combinations to be experimentally tested, then reducing the subsequent membrane characterizations.

Future improvements could be directed toward the incorporation of this thermo-kinetic coupled approach into phase field or dissipative particle dynamics models, as well as the use of a CahnHilliard kinetics and the description of the convective movement of the polymer. Despite the extra computational cost, these improvements would allow a more rigorous phenomenological description of the NIPS phenomena and therefore a more realistic prediction of the membrane morphology, that could account for the variability of the polymer fraction values observed in the SEM image profiles of real membranes.

Data Availability Statement

All required data are included in the article and/or in the Supporting Information. The data that support the findings of this study are available from the corresponding author upon reasonable request.

Conflicts of Interest

The authors declare no conflicts of interest.

Funding

This research was funded by the Spanish Research Agency through the projects PCI2018-092929/AEI/10.13039/501100011033 (call APCIN 2018), PID2019-105827RB-I00/AEI/10.13039/501100011033, and PDC2022-133704-I00_MCIN/AEI/10.13039/501100011033 and UE Next GenerationEU/PRTR. Marta Romay is grateful to the FPI contract grant (BES-2017-081112).

Supporting Information

Additional supporting information can be found online in the Supporting Information section. (*Supporting Information*) Supporting Information includes complementary procedures, mathematical model details, MATLAB code, figures, and tables collected on the following Appendices: Appendix A: Flory–Huggins thermodynamic model for quaternary systems; Appendix B: determination of binary interaction parameters based on Hansen solubility parameters (HSP); Appendix C: UNIFAC-Dortmund methodology; Appendix D: binodal curve linearization; Appendix E: numerical discretization of the thermo-kinetic model; Appendix F: SEM image processing computational methodology; Appendix G: complementary information for discussion of results.

References

[1] J. D. Enderle and J. D. Bronzino, *Introduction to Biomedical Engineering* (Elsevier/Academic Press, Burlington, Massachusetts, 3rd edition, 2011).

[2] N. Diban and D. Stamatialis, "Polymeric Hollow Fiber Membranes for Bioartificial Organs and Tissue Engineering Applications," *Journal of Chemical Technology & Biotechnology* 89, no. 5 (2014): 633–643.

[3] M. Mantecón-Oria, O. Tapia, M. Lafarga, et al., "Influence of the Properties of Different Graphene-Based Nanomaterials Dispersed in Polycaprolactone Membranes on Astrocytic Differentiation," *Scientific Reports* 12, no. 1 (2022).

[4] S. Sánchez-González, N. Diban, F. Bianchi, H. Ye, and A. Urtiaga, "Evidences of the Effect of GO and rGO PCL Membranes on the Differentiation and Maturation of Human Neural Progenitor Cells," *Macromolecular Bioscience* 18 (2018): 1–8.

[5] S. Mohsenpour, S. Leaper, J. Shokri, M. Alberto, and P. Gorgojo, "Effect of Graphene Oxide in the Formation of Polymeric Asymmetric Membranes via Phase Inversion," *Journal of Membrane Science* 641 (2022): 119924.

[6] S. Mazinani, S. Darvishmanesh, A. Ehsanzadeh, and B. Van der Bruggen, "Phase Separation Analysis of Extem/Solvent/Non-Solvent Systems and Relation With Membrane Morphology," *Journal of Membrane Science* 526 (2017): 301–314.

[7] S. P. Nunes, P. Z. Culfaz-Emecen, G. Z. Ramon, et al., "Thinking the Future of Membranes: Perspectives for

Advanced and New Membrane Materials and Manufacturing Processes," *Journal of Membrane Science* 598 (2020): 117761.
[8] Y. Tang, Y. Lin, D. M. Ford, et al., "A Review on Models and Simulations of Membrane Formation via Phase Inversion Processes," *Journal of Membrane Science* 640 (2021): 119810.
[9] K. V. Kurada and S. De, "Modeling of Solution Thermodynamics: A Method for Tuning the Properties of Blend Polymeric Membranes," *Journal of Membrane Science* 540 (2017): 485–495.
[10] Y.-M. Wei, Z.-L. Xu, X.-T. Yang, and H.-L. Liu, "Mathematical Calculation of Binodal Curves of a Polymer/Solvent/Nonsolvent System in the Phase Inversion Process," *Desalination* 192, no. 1–3 (2006): 91–104.
[11] L. Xu and F. Qiu, "Simultaneous Determination of Three Flory-Huggins Interaction Parameters in Polymer/Solvent/Nonsolvent Systems by Viscosity and Cloud Point Measurements," *Polymer* 55, no. 26 (2014): 6795–6802.
[12] G. R. Fernandes, J. C. Pinto, and R. Nobrega, "Modelling and Simulation of the Phase-Inversion Process During Membrane Preparation," *Journal of Applied Polymer Science* 82, no. 12 (2001): 3036–3051.
[13] T. Ahmad, L. M. Rehman, R. Al-Nuaimi, et al., "Thermodynamics and Kinetic Analysis of Membrane: Challenges and Perspectives," *Chemosphere* 337 (2023): 139430.
[14] M. A. Khansary, A. Marjani, and S. Shirazian, "On the Search of Rigorous Thermo-Kinetic Model for Wet Phase Inversion Technique," *Journal of Membrane Science* 538 (2017): 18–33.
[15] P. Radovanovic', S. W. Thiel, and S.-T. Hwang, "Formation of Asymmetric Polysulfone Membranes by Immersion Precipitation," *Part I. Modelling Mass Transport during Gelation* (1992).
[16] I. V. Maggay, M.-L. Yu, D.-M. Wang, C.-H. Chiang, Y. Chang, and A. Venault, "Strategy to Prepare Skin-Free and Macrovoid-Free Polysulfone Membranes via the NIPS Process," *Journal of Membrane Science* 655 (2022): 120597.
[17] K. V. Kurada, A. Agarwal, and S. De, "Effect of Mixed Solvents on Phase Inversion of Polymeric Membranes," *Polymer International* 69, no. 10 (2020): 920–932.
[18] W.-L. Hung, D.-M. Wang, J.-Y. Lai, and S.-C. Chou, "On the Initiation of Macrovoids in Polymeric Membranes - Effect of Polymer Chain Entanglement," *Journal of Membrane Science* 505 (2016): 70–81.
[19] M. Romay, N. Diban, and A. Urtiaga, "Thermodynamic Modeling and Validation of the Temperature Influence in Ternary Phase Polymer Systems," *Polymers* 13, no. 5 (2021): 1–20.
[20] N. Diban, S. Sánchez-González, M. Lázaro-Díez, J. Ramos-Vivas, and A. Urtiaga, "Facile Fabrication of Poly(ε-Caprolactone)/Graphene Oxide Membranes for Bioreactors in Tissue Engineering," *Journal of Membrane Science* 540 (2017): 219–228.
[21] Z. Wang, J. Lin, D. Zhang, et al., "Porous Morphology and Mechanical Properties of Poly(lactide-Co-Glycolide) Hollow Fiber Membranes Governed by Ternary-Phase Inversion," *Journal of Membrane Science* 579 (2019): 180–189.
[22] M. Hopp-Hirschler, *Modeling of Porous Polymer Membrane Formation* (Universität Stuttgart, 2017).
[23] R. M. Boom, T. van den Boomgaard, J. W. A. van den Berg, and C. A. Smolders, "Linearized Cloudpoint Curve Correlation for Ternary Systems Consisting of One Polymer, One Solvent and One Non-Solvent," *Polymer* 34, no. 11 (1993): 2348–2356.
[24] A. V. Patsis, E. H. Henriques, and H. L. Frisch, "Interdiffusion in Complex Polymer Systems Used in the Formation of Microporous Coatings," *Journal of Polymer Science Part B: Polymer Physics* 28, no. 13 (1990): 2681–2689.
[25] M. Sadrzadeh and S. Bhattacharjee, "Rational Design of Phase Inversion Membranes by Tailoring Thermodynamics and Kinetics of Casting Solution Using Polymer Additives," *Journal of Membrane Science* 441 (2013): 31–44.
[26] G. K. Reddy, B. A. Sahitya, and A. Ghosh, "Size Analysis of Brain Tumor from MRI Images Using MATLAB," *2021 12th International Conference on Computing Communication and Networking Technologies, ICCCNT* (2021): 1–5.
[27] T.-H. Young, L.-P. Cheng, C.-C. Hsieh, and L.-W. Chen, "Phase Behavior of EVAL Polymers in Water-2-Propanol Cosolvent," *Macromolecules* 31, no. 4 (1998): 1229–1235.
[28] B. A. Wolf and R. J. Molinari, "True Cosolvency," *Die Makromolekulare Chemie* 173, no. 1 (1973): 241–245.
[29] V. V. Perera, N. L. Fernando, B. Nissanka, and D. R. Jayasundara, "In Situ Real Time Monitoring of Hygroscopic Properties of Graphene Oxide and Reduced Graphene Oxide," *Adsorption-Journal of the International Adsorption Society* 25, no. 8 (2019): 1543–1552.
[30] M. Asgarpour Khansary, M. A. Aroon, A. Marjani, and S. Shirazian, "A Priority Supposition for Estimation of Time-Dependent Changes in Thickness and Weight of Polymeric Flat Sheet Membranes Fabricated by the Nonsolvent Induced Phase Separation (NIPS) Technique," *Advances in Polymer Technology* 37, no. 6 (2018): 1963–1969.
[31] M. Safarpour, V. Vatanpour, and A. Khataee, "Preparation and Characterization of Graphene Oxide/TiO2 Blended PES Nanofiltration Membrane With Improved Antifouling and Separation Performance," *Desalination* 393 (2016): 65–78.